SAND2020-14066J

Hydrogen-Assisted Fracture Resistance of Pipeline Welds in Gaseous Hydrogen

Joseph A. Ronevich*[1], Eun Ju Song[1], Brian P. Somerday[2], Christopher W. San Marchi[1]

[1]Sandia National Laboratories, 7011 East Avenue, Livermore, CA 94550, USA
[2]Somerday Consulting, LLC, 118 Rehoboth Rd., Wayne, PA, USA

Abstract

Fracture resistance of pipeline welds from a range of strength grades and welding techniques was measured in air and 21 MPa hydrogen gas, including electric resistance weld of X52, friction stir weld of X100 and gas metal arc welds (GMAW) of X52, X65 and X100. Welds exhibited a decrease in fracture resistance in hydrogen compared to complementary tests in air. A general trend was observed that fracture resistance in 21 MPa hydrogen gas decreased with increasing yield strength. To accommodate material constraints, two different fracture coupon geometries were used in this study, which were shown to yield similar fracture resistance values in air and 21 MPa hydrogen gas; values using different coupons resulted in less than 15% difference. In addition, fracture coupons were removed from controlled locations in select welds to examine the potential influence of orientation and residual stress. The two orientations examined in the X100 GMAW exhibited negligible differences in fracture resistance in air and, similarly, negligible differences in hydrogen. Residual stress exhibited a modest influence on fracture resistance; however, a consistent trend was not observed between tests in air and hydrogen, suggesting further studies are necessary to better understand the influence of residual stress. A comparison of welds and base metals tested in hydrogen gas showed similar susceptibility to hydrogen-assisted fracture. The overall dominant factor in determining the susceptibility to fracture resistance in hydrogen is the yield strength.

Keywords: Hydrogen embrittlement, fracture toughness, pipelines, welds.

1. Introduction

Large-scale hydrogen utilization is gaining favor to support renewable energy technologies. Significant barriers, however, still exist in establishing large-scale hydrogen storage and distribution infrastructure. Fabrication and installation of an entirely new pipeline infrastructure dedicated to hydrogen is currently cost-prohibitive. The other alternative is to utilize existing infrastructure. For any pipeline system intended for hydrogen distribution (including distribution of blends), an evaluation of the materials compatibility with hydrogen gas system should be performed. In order to ensure the integrity of a hydrogen pipeline, ASME B31.12 [1] requires a fracture assessment, which includes understanding the fatigue crack growth rate (FCGR) behavior and the fracture resistance (K_{JH}) for the materials of construction in a gaseous hydrogen environment. Numerous studies [2-8] have addressed the fatigue behavior of pipeline steels in high-pressure gaseous hydrogen environments. In short, it has been shown that FCGR is accelerated in hydrogen gas by over an order of magnitude compared to air. Studies have also shown that hydrogen-assisted FCGR appears to be insensitive to strength of the pipeline steel, as similar FCGR were measured in steels with specified minimum yield strengths (SMYS) ranging from 358 to 700 MPa, essentially X52 to X100 steel grades [9]. Recent studies [9-15] have examined the FCGR behavior of pipeline steel welds in hydrogen gas and have demonstrated that, in general, the welds behave similarly to the base metals if residual stresses are accounted for.

Although FCGR data for base metals and welds in high-pressure hydrogen gas appear to be bounded by recent studies [2-15], one significant unknown is the fracture resistance behavior of pipeline steel

welds in hydrogen gas. Fracture toughness is the measurement of material resistance to crack extension under monotonically increasing loading and is an important mechanical property that is needed for pipeline integrity management. In this paper, we use the term fracture resistance (K_{JH}) as opposed to plane-strain fracture toughness (K_{JIC}) when discussing hydrogen effects to emphasize that fracture resistance is not a material property like K_{JIC} but rather dependent on the environment. Several studies [6, 7, 16, 17] were conducted on a variety of pipeline steel grades in high-pressure hydrogen gas, which established base metal fracture resistance behavior in hydrogen. Unlike hydrogen-accelerated FCGR, the trends from the literature [6, 7, 16-18] suggest that hydrogen-assisted fracture resistance depends on strength, where K_{JH} decreases with increasing strength.

Welds are always of concern when integrity is being considered in design or recertification. Welds have the potential to possess unique strength, microstructure, macro-scale defects, and residual stresses compared to the parent base metal. There is a noticeable gap in fracture resistance data for pipeline steel welds in gaseous hydrogen in the literature, which is the motivation for this paper. Several studies [15, 19-24] have examined the fracture behavior of pipeline steel welds; however, these studies have not provided a broad overview of the behavior of welds. Testing capabilities to perform high pressure hydrogen tests are limited and challenges associated with extracting test coupons from localized regions (such as welds) have both likely contributed to the lack of published data. In this paper, the fracture resistance in gaseous hydrogen is examined for a variety of pipeline steel welds ranging in welding techniques and strengths. Two different test coupon geometries were used to generate the fracture data to assess the reliability of test results, which yielded similar fracture resistance values.

2. Experimental Procedures

2.1 *Welded Pipes*

The pipeline steels examined in this study were all API 5L grades designated by an ‘X’ followed by the specified minimum yield strength (SMYS), so for example an X52 steel grade has a SMYS of 52 ksi (358 MPa). Commercially produced steel pipes were welded using different welding techniques, of which the details can be found in previous work [8, 10, 11, 13, 14, 25]. An overview of the dimensions of the welded pipes can be found in Table 1. Fracture testing was conducted on the following steel grades and welds:

- Modern X52 (fabricated in 1990s/2000s) with an electric resistance seam weld (X52 ERW) [8]
- Vintage X52 (fabricated in 1960s) with a gas metal arc girth weld (X52 GMAW-V) [14]
- X65 with gas metal arc girth weld (X65 GMAW) [13, 25]
- X100 gas metal arc girth weld (X100 GMAW) [10, 11]
- X100 friction stir seam weld (X100 FSW) [10].

The X100 GMAW and X100 FSW were fabricated using the same X100 base metal [10]. The chemical compositions of the base metals are listed in Table 2 along with the composition of the X52 GMAW-V. Chemical compositions were not measured for the other welds, however, the composition of the X52 ERW and X100 FSW can be assumed to be identical to the parent metal, as filler metal is not used for these welding practices. These materials were selected for this study because they represent a diverse set of pipeline grades and welding techniques.

The base metal microstructures have been well characterized in previous work [8, 10, 13, 14]. The two X52 base metals [8, 14] and X65 base metal [13] contain a ferrite-pearlite microstructure whereas the X100 base metal [10] contains a bainite-ferrite microstructure. Although a detailed assessment of the weld microstructures was not performed in this study, the following lists the predominant microstructures in the various welds tested. In general, the microstructure of the weld was finer than the parent base metal.

- X52 ERW – ferrite with dispersed or aligned carbides
- X52 GMAW-V – polygonal and acicular ferrite, some tempered martensite [14]
- X65 GMAW – grain boundary and Widmanstatten ferrite, ferrite with aligned second phase [13]
- X100 GMAW – grain boundary, polygonal, and acicular ferrite [10]
- X100 FSW – grain boundary and bainitic ferrite, with some regions of martensite [10]

2.2 Fracture Test Coupons

Two different fracture coupons were used in this study: arc-shaped tension and compact tension coupons. The arc-shaped tension (arc) coupon is defined in ASTM E399 [26], whereas the compact tension (CT) is defined in ASTM E1820 [27]. Drawings of the two coupons are shown in Fig. 1; note the arc coupon is modified from the standard by machining the pin holes further from the edge of the coupon to reduce the likelihood of failure at the pin holes. The arc coupon offers significant advantages over the CT in that it is smaller and can be extracted in desirable orientations from welds. The arc coupon has a width (W) of 9.1 mm and thickness (B) of 4.5 mm. Side-grooves were machined prior to precracking along the crack plane, which resulted in a net thickness that was 15% less than the gross thickness. Arc coupons can be extracted such that the crack extends in the radial direction of the pipe provided its thickness exceeds 14 mm, whereas practically-sized CT coupons cannot be extracted in this orientation due to width (W) requirements. In this study, the CT coupons have dimensions of W = 26.5 mm and gross thickness (B) of either 9.5 mm or 12.7 mm. Side-grooves were machined prior to precracking along the crack plane, which resulted in a net thickness that was 12% less than the gross thickness. A schematic of the 5 different welds along with the corresponding tensile and fracture coupon extraction orientations are shown in Fig. 2. More description of the tensile coupons is found in the subsequent section. In the X65 GMAW, X100 GMAW, and X100 FSW, arc fracture coupons were extracted such that the crack extended radially in the pipe wall and the loading direction was transverse to the welding direction (LR orientation in the conventional nomenclature [26]). In the X52 GMAW-V, the thickness of the pipe (10.6 mm) did not permit this orientation, therefore the arc coupon was oriented such that the loading axis was transverse to the welding direction, but the crack direction was parallel to the welding direction (e.g. circumferential) as shown in Fig. 2b (LC orientation). CT coupons were oriented in the X52 ERW with the crack propagation direction parallel to the welding direction (longitudinal) and loading axis transverse to the weld (e.g. circumferential) as shown in Fig. 2a. In the X65 GMAW, two arc fracture coupons were extracted in the same orientation (LR) but were separated within the weld biased towards either the weld root (Loc-A) or cover pass (Loc-B) as shown in Fig. 2c. The motivation for extracting in these two locations was to examine potential effects of residual stress, as previous work [13, 25] showed a large residual stress gradient in the radial direction of the X65 GMAW. Finally, fracture coupons were extracted in two different orientations (LR and LC) from the X100

GMAW (as shown in Fig. 2d) in order to examine the effect of cracking direction. They were designated as X100 GMAW LC and X100 GMAW LR.

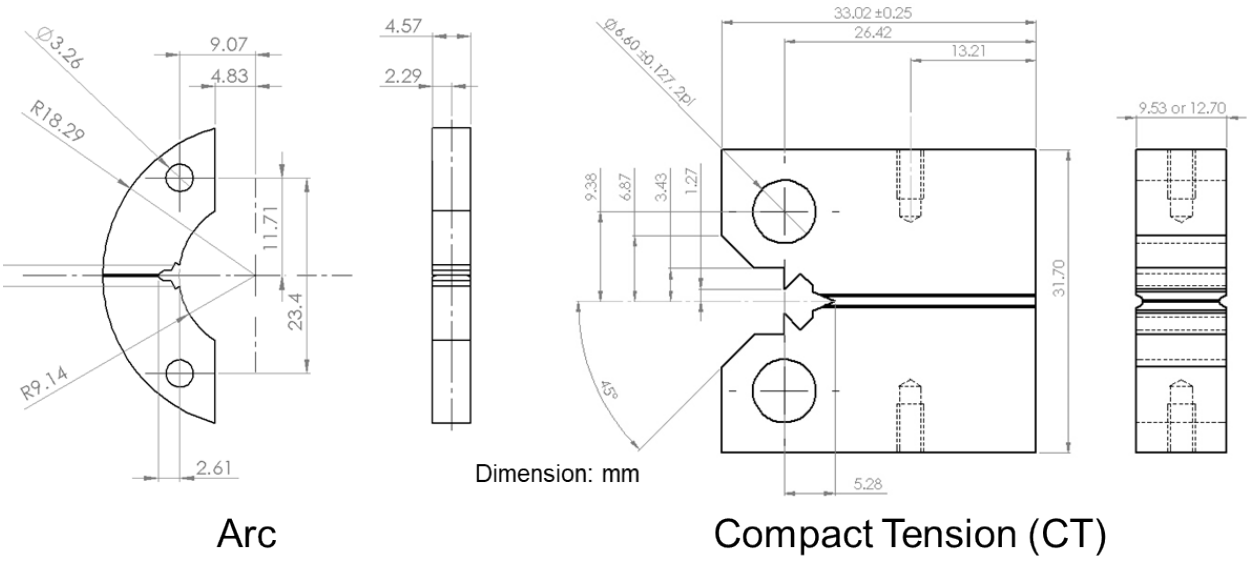

Figure 1 – Drawings of arc-shaped tension (arc) and compact tension (CT) test geometry for fracture testing. Dimensions are in mm.

In addition to extraction of fracture coupons from the welds, arc and CT coupons were also extracted from the X100 base metal in the CL orientation, meaning the loading axis is in the circumferential direction and the crack extends in the longitudinal direction. Fracture resistance was measured and compared from these two different test coupons to evaluate similitude of fracture resistance results between the arc and CT geometries.

2.3 Tensile test coupons

The tensile properties of the welds are provided in Table 3 for tests performed in air. It should be noted that yield and tensile strength are not observed to change when tested in hydrogen gas in ferritic pipeline steels; however, total elongation and reduction of area are often reduced [28]. The mechanical properties were obtained largely from previous studies on these same welds and reported in the literature [8, 10, 11, 14, 25]. In most cases, tensile coupons were removed perpendicular to the welding direction, such that the gauge section was fully contained within the weld [10, 25], e.g. X100 FSW, X100 GMAW, X65 GMAW. Therefore, the yield and tensile strengths represent the same orientation as the loading direction of fracture tests. The X52 GMAW-V tensile coupon, in contrast, was removed parallel to the girth weld direction, and fully contained within the weld [14]. The mechanical properties of the X52 [8] and X65 [25] base metals were obtained in the longitudinal direction in contrast to the X100 base metal [11], which was measured in the circumferential direction. The tensile properties of the X52 ERW were not measured, therefore the properties are only listed for the X52 base metal in the longitudinal direction, which is parallel to the seam weld. In lieu of measuring tensile properties of the X52 ERW and due to the small size of the welded zone, microhardness was measured across the weld zone as shown in Fig. 3. The microhardness of the welded region is about 10% higher than the base metal.

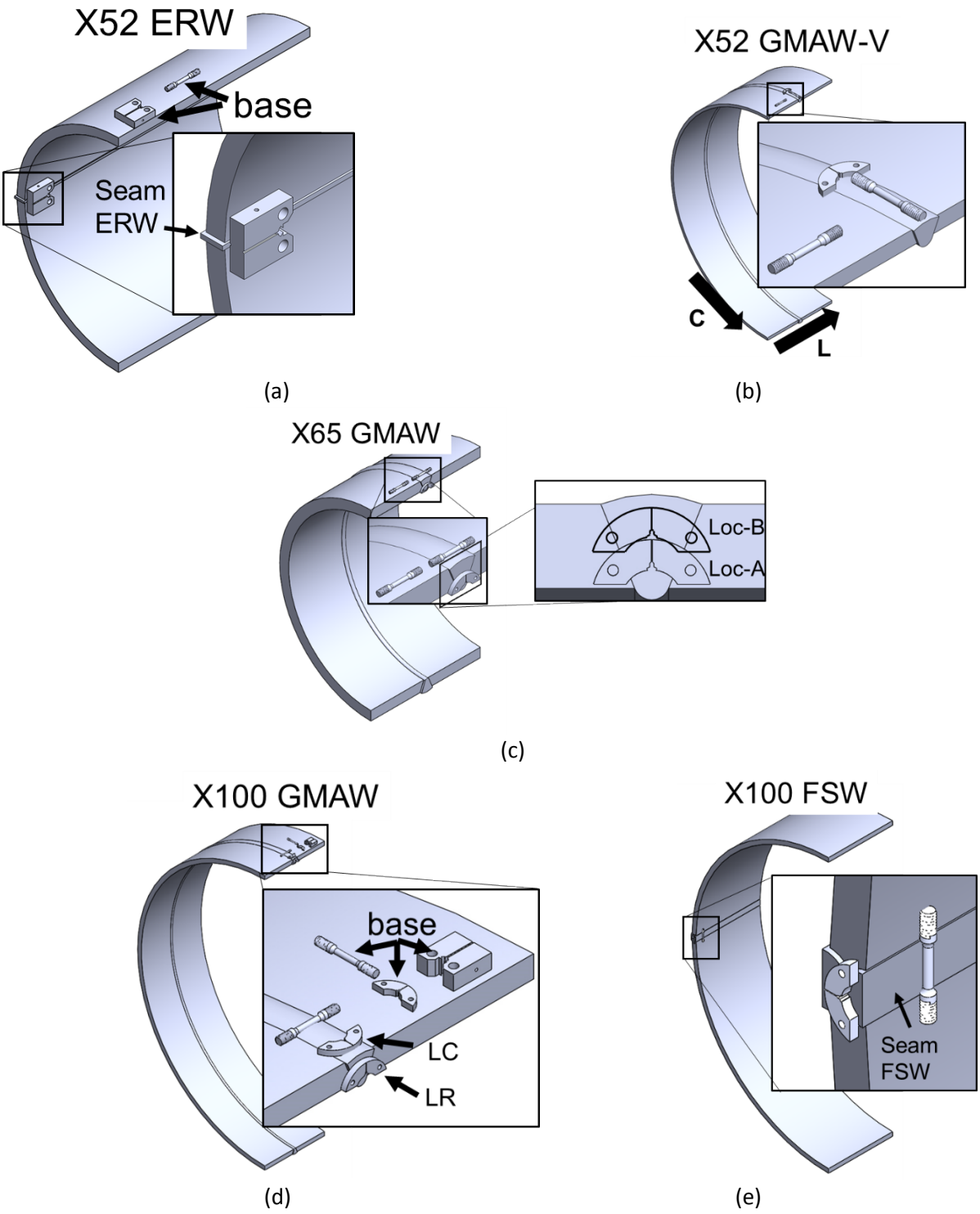

Figure 2 – Schematics of approximate locations of fracture and tensile coupons from welded pipes: (a) X52 ERW, (b) X52 GMAW-V, (c) X65 GMAW, (d) X100 GMAW, and (e) X100 FSW. Coupons are shown to demonstrate orientation only, not exact position in the welds. In general, coupons were extracted from mid-thickness of the weld except in X65 GMAW where fracture coupons were biased towards root and top of weld, as shown in Fig 2c.

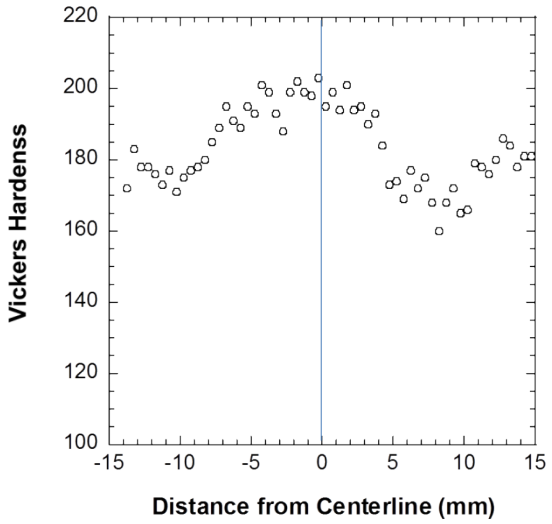

Figure 3 – Microhardness trace across the X52 ERW seam. Approximately 10% higher hardness was measured along the ERW centerline compared to remote hardness in base metal at 15 mm.

2.4 Rising Displacement Fracture Resistance Tests

Rising displacement fracture resistance tests were performed on the arc and CT fracture coupons in air and 21 MPa hydrogen gas. Prior to performing each fracture test, a precrack was extended in air from the starter notch to an a/W range between 0.5 and 0.6, where 'a' is the crack depth from the load line. The final maximum stress intensity factor (K_{max}) at the end of the precrack was controlled to be less than 20 MPa $m^{1/2}$. CT coupons were tested according to ASTM E1820 [27] under actuator displacement control. The arc geometry was standardized for linear elastic fracture mechanics (ASTM E399 [26]), but an elastic-plastic analysis was performed consistent with ASTM E1820 [27]. Previous work [29] evaluated the validity of elastic-plastic analysis on the arc test specimen geometry through finite element modeling. It was determined that using the η-values consistent with the CT test specimen geometry in ASTM E1820 [27] for analysis with the arc test specimen geometry would result in reliable results for the calculation of J [29]. In using ASTM E1820 [27], the calculation of a J-integral vs crack extension curve (e.g. J-R curve) requires calculating a J_{total} value which is broken into elastic (J_{el}) and plastic (J_{pl}) components, $J_{total} = J_{el} + J_{pl}$. The J_{pl} term is defined to be $J_{pl} = \frac{\eta A_{pl}}{B_N b_o}$, where η is a geometry factor, A_{pl} is the area under the force vs displacement curve, B_N is net thickness, and b_o is remaining ligament equal to W-a_o. In this study, the η used for the arc was the same as defined for a CT specimen, which can be found in ASTM E1820 [27] as $\eta = 2 + 0.522b_o/W$. To confirm the assessment from the literature, arc and CT coupons were extracted from the X100 base metal in the CL orientation and tested in air and 21 MPa hydrogen gas to compare the fracture resistance values between the two geometries.

Fracture tests were performed in-situ in 21 MPa hydrogen gas in a custom-built pressure vessel fixtured on a commercial servo-hydraulic load frame. The system is equipped with an internal load cell for monitoring the applied load and a clip gauge is mounted on the coupon to monitor load-line displacement (LLD). Arc coupon fracture tests were performed at a constant actuator displacement rate of 0.005 mm/min. CT coupon fracture tests on the X52 ERW were performed at 0.033 mm/min and

0.003 mm/min; however, a negligible difference was observed in the measured fracture resistance at these test rates. The CT fracture tests on the X100 base metal were performed at 0.005 mm/min. For all tests, displacement rates were monotonic and the crack position was monitored using the direct current potential difference (DCPD) technique according to procedures outlined in ASTM E1820 [27]. Fracture tests were terminated when load decreased by more than 10%. More details of the experimental setup and unique attributes of testing in high-pressure gaseous hydrogen can be found in [30].

After termination of the test and removal from the high-pressure apparatus, coupons were heat tinted at 275°C for 30 minutes to mark the location of crack extension and then were fatigue cycled to separate the fracture surfaces into two pieces. For the data analysis, crack initiation was determined when the DCPD voltage deviated from a baseline linear trend in a DCPD vs LLD plot as shown in Fig. 4a. To verify the crack initiation point, a fracture test (X100 GMAW LR, specimen number a5) was interrupted just beyond the presumed crack initiation and compared to a complete fracture test (X100 GMAW LR, specimen number a3), both tested in hydrogen at a pressure of 21 MPa. The fracture coupons were heat-tinted to mark the extent of crack extension and then fatigue cycled to separate the fracture surfaces. Images of the fracture surfaces are shown in Fig. 4b. It is clear that crack extension occurred in the interrupted fracture test, demonstrating that initiation is characterized by the first deviation of the DCPD signal from the baseline linear trend (dashed line in Fig. 4a).

An elastic-plastic fracture mechanics (EPFM) analysis was performed according to ASTM E1820 [27] to construct the crack growth resistance (J-R) curve (J-integral vs crack extension, Δa). A 0.2 mm-offset construction line was established based on the flow stress (S_Y = average of yield and tensile stress) of each material. The intersection of the J-R curve and the 0.2 mm-offset construction line determined the provisional fracture resistance (J_Q). In order for J_Q to represent a size-independent value of fracture resistance J_{IC} according to ASTM E1820 [27], two dimensional criteria must be satisfied:

$$B > 10J_Q/S_Y \text{ and } b_o > 10J_Q/S_Y \qquad (1)$$

where B is thickness of the test coupon, S_Y is the flow stress, and b_o is the remaining uncracked ligament. All measured J_Q values satisfied these two criteria except for two tests in air on X65 GMAW Loc-B (arc specimens). The size-independent fracture resistance measured in gaseous hydrogen is referred to as J_H. Values of the elastic-plastic J can be converted to equivalent linear-elastic K values according to equation 2:

$$K_{JIC} = \sqrt{\frac{EJ_{IC}}{1-\nu^2}} \qquad \text{or} \qquad K_{JH} = \sqrt{\frac{EJ_H}{1-\nu^2}} \qquad (2)$$

where E is elastic modulus (E = 207 GPa) and ν is Poisson's ratio of 0.3. For tests performed in air, we use K_{JIC} to describe a value of K converted from a measurement of J_{IC}. Similarly, K_{JH} is used to describe the measurements performed in hydrogen gas and represents an environment-dependent fracture resistance (in this case fracture resistance in gaseous hydrogen at pressure of 21 MPa).

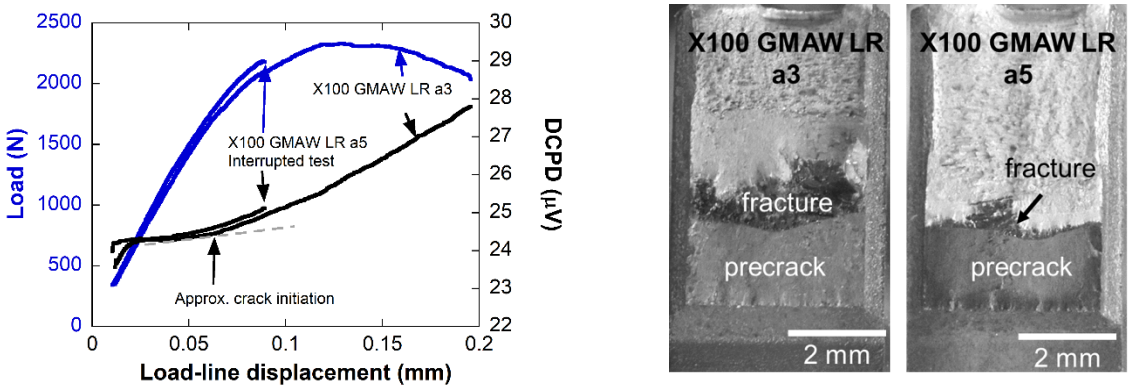

(a) (b)

Figure 4 – (a) Load and direct current potential difference (DCPD) vs load-line displacement for an interrupted arc fracture test (X100 GMAW LR a5) and complete fracture test (X100 GMAW LR a3) in hydrogen at pressure of 21 MPa. The interrupted test was terminated when DCPD values deviated from the baseline linear trend (dashed line) signifying crack initiation. (b) Heat-tinted fracture surfaces of the coupons from (a).

3. Results

The fracture toughness (air) and fracture resistance (gaseous hydrogen at pressure of 21 MPa) of the base metals and the welds are summarized in Fig. 5 as a function of yield strength for all the testing described in this study. The results from the individual tests are shown in Appendix A. The following sub-sections will discuss the details of the results found in Fig. 5.

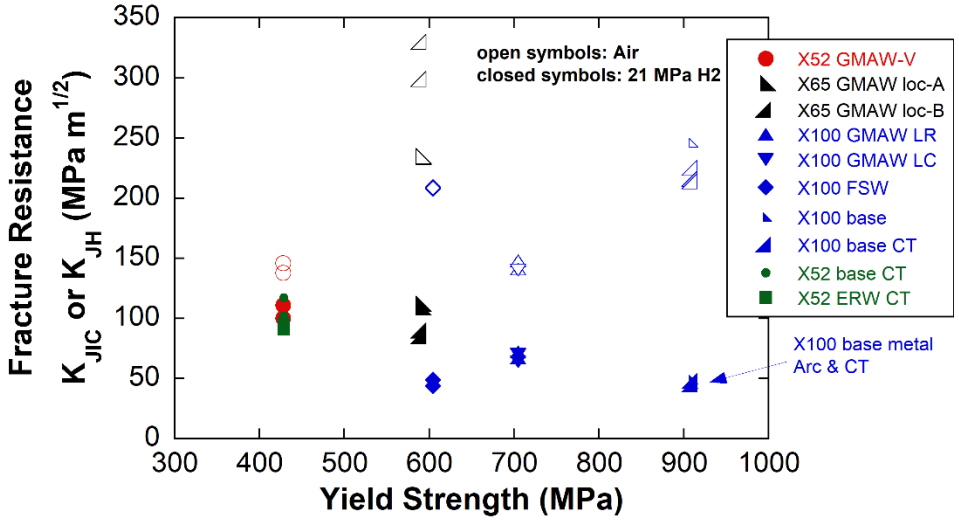

Figure 5 – Fracture toughness in air (K_{JIC}) and Fracture resistance in hydrogen gas at pressure of 21 MPa (K_{JH}) as a function of yield strength of the material. Open symbols represent tests in air, and closed symbols represent tests in 21 MPa H_2. The materials that were tested using CT coupons are noted in the legend, other results derive from the arc geometry. Note that yield strength of X52 ERW was not measured; therefore, it is plotted at same yield strength as base metal even though microhardness of X52 ERW was 10% higher than X52 base metal suggesting that it has a higher yield strength than the X52 base metal.

3.1 *Test coupon configuration and crack orientation (X100 GMAW)*

J-R curves (e.g. J-integral vs crack extension) are shown in Fig. 6a for replicate tests of both the arc and CT coupons of X100 base metal in gaseous hydrogen at pressure of 21 MPa. All coupons in Fig. 6a are oriented in the CL orientation. While there is some variation in the slopes of the curves at larger crack extensions, the J_{QH} values (e.g. intersection with 0.2 mm-offset construction line) are consistent. When converted to values of K according to equation 2, the fracture resistance (K_{JH}) of the CT test coupons is 45 and 48 MPa $m^{1/2}$ for duplicate tests; in comparison the arc coupon yielded K_{JH} values of 45 and 49 MPa $m^{1/2}$. These four values are within less than ±5% and the average value is 47 MPa $m^{1/2}$ for both coupons. Similarly, J-R curves are shown in Fig. 6b for both geometries tested in air. Values of K_{JIC} for the CT coupons were 225, 216, and 214 MPa $m^{1/2}$, whereas for the arc coupon, a K_{JIC} value of 246 MPa $m^{1/2}$ was measured from a single test. These represent a maximum difference of 15%. This comparison at the higher K-value range in air is based on only a single arc coupon and therefore may not fully capture the trends between arc and CT specimens with higher fracture toughness.

Arc coupons were extracted in two different orientations for the X100 GMAW as shown in Fig. 2 (LR and LC). The fracture toughness in air was nearly identical for the LR and LC orientations: K_{JIC} = 145 MPa $m^{1/2}$ and K_{JIC} = 140 MPa $m^{1/2}$ respectively. Similarly, the fracture resistance values in 21 MPa hydrogen gas were essentially the same for the two orientations: K_{JH} = 70 MPa $m^{1/2}$ and K_{JH} = 67 MPa $m^{1/2}$ for the LR and LC orientations respectively. These values represent the average of duplicate tests. Individual test results can be found in Appendix A.

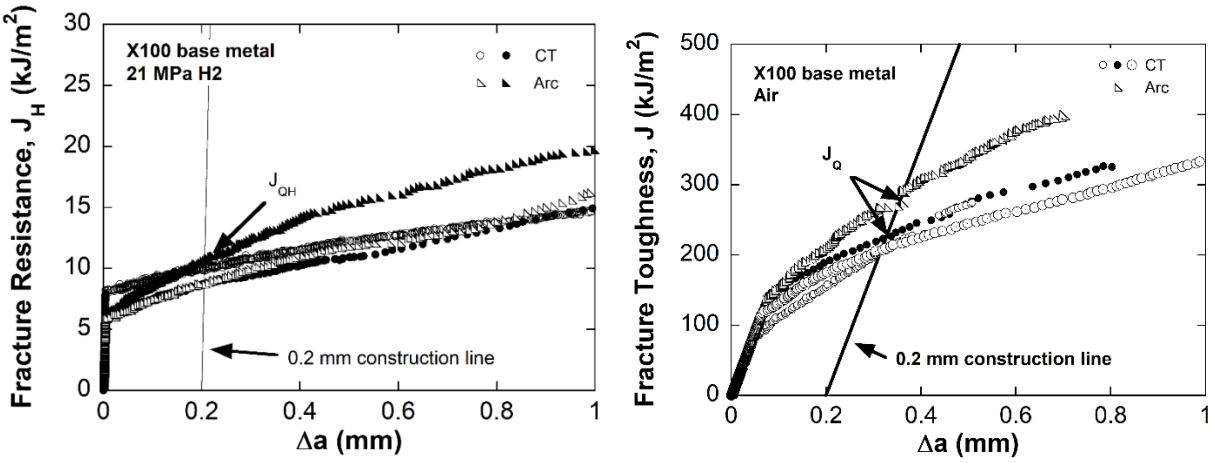

Figure 6 - Comparison of X100 base metal arc and CT coupons (a) fracture resistance in 21 MPa hydrogen gas and (b) fracture toughness in air.

3.2 Specimen location (X65 GMAW)

Fracture of the X65 GMAW was evaluated at two locations in the weld (Fig. 2c), using the arc coupon. Tests were performed both in air and 21 MPa hydrogen gas. Coupons extracted from Loc-A displayed fracture toughness (in air) of 235 MPa $m^{1/2}$, compared to fracture toughness of 315 MPa $m^{1/2}$ in Loc-B. The toughness values at Loc-B violate the dimensional validity criteria according to equation 1; therefore, these values are reported as size-dependent K_{JQ} values. In contrast, testing in hydrogen resulted in higher fracture resistance at Loc-A compared to Loc-B in the X65 GMAW: K_{JH} = 111 MPa $m^{1/2}$ and K_{JH} = 88 MPa $m^{1/2}$ for Loc-A and Loc-B respectively, which represents a difference of approximately

26%. These values are the average of duplicate tests and exhibited good repeatability with the variability less than ±3 MPa $m^{1/2}$ (except the Loc-A in air, which showed greater variation, in addition to not satisfying the size criteria of the standard).

3.3 Welding practice (X52 GMAW, X65 GMAW vs X52 ERW; X100 GMAW vs FSW)

The fracture resistance was 106 MPa $m^{1/2}$ (average of duplicate tests) for the X52 GMAW-V in gaseous hydrogen at pressure of 21 MPa. The X52 ERW exhibited a slightly lower fracture resistance of 94 MPa $m^{1/2}$ in hydrogen. The X52 ERW fracture toughness was not measured in air; however, the X52 GMAW-V arc coupons exhibited lower fracture toughness (K_{JIC} = 142 MPa $m^{1/2}$) compared to welds with strengths less than 600 MPa yield strength (e.g. X65 GMAW had K_{JIC} > 235 MPa $m^{1/2}$ in air). It appears that the effect of hydrogen on fracture of the X52 GMAW-V, however, was comparatively less than for the other welds, which will be described further in the Discussion. The K_{JH} values are similar to the fracture resistance of the X52 base metal in gaseous hydrogen at the same pressure: 104 MPa $m^{1/2}$ (average of 4 tests). Similarly, as mentioned above, the X65 GMAW fracture resistance values in hydrogen were 111 and 88 MPa $m^{1/2}$ for Loc-A and loc-B, respectively.

The fracture resistance of the X100 GMAW LR and LC were 70 and 67 MPa $m^{1/2}$, respectively, in hydrogen as mentioned previously. The X100 FSW displayed a 30% lower fracture resistance with an average value of duplicate tests of K_{JH} = 47 MPa $m^{1/2}$ compared to the X100 GMAW, but the same as the X100 base metal (47 MPa $m^{1/2}$). In air, the fracture toughness of the X100 FSW is 209 MPa $m^{1/2}$, which is similar to the average value (220 MPa $m^{1/2}$) for the X100 base metal measured in air from the arc coupons representing only a 5% difference.

3.4 Fracture surface evaluation

Following the fracture tests, the fracture surfaces of the welds tested in 21 MPa hydrogen gas were examined in a scanning electron microscope and representative fracture surface images from select welds are shown in Fig. 7. The predominant fracture feature in the welds tested in 21 MPa hydrogen gas was transgranular fracture with evidence of micro-scale plasticity. Microvoid coalescence is apparent in locations on some of the fracture surfaces. For comparison, representative fracture surfaces of X52 GMAW-V and X100 GMAW fractured in air are shown in Fig. 8. The fracture surfaces in air show predominantly ductile microvoid coalescence. Inclusions as large as 20 μm are observable on the fracture surfaces of the X52 GMAW-V coupons, both tested in air (Fig. 8a) and hydrogen (Fig. 7a). These inclusions contain Mn, S, O, and Si, as identified via energy dispersive spectroscopy (EDS).

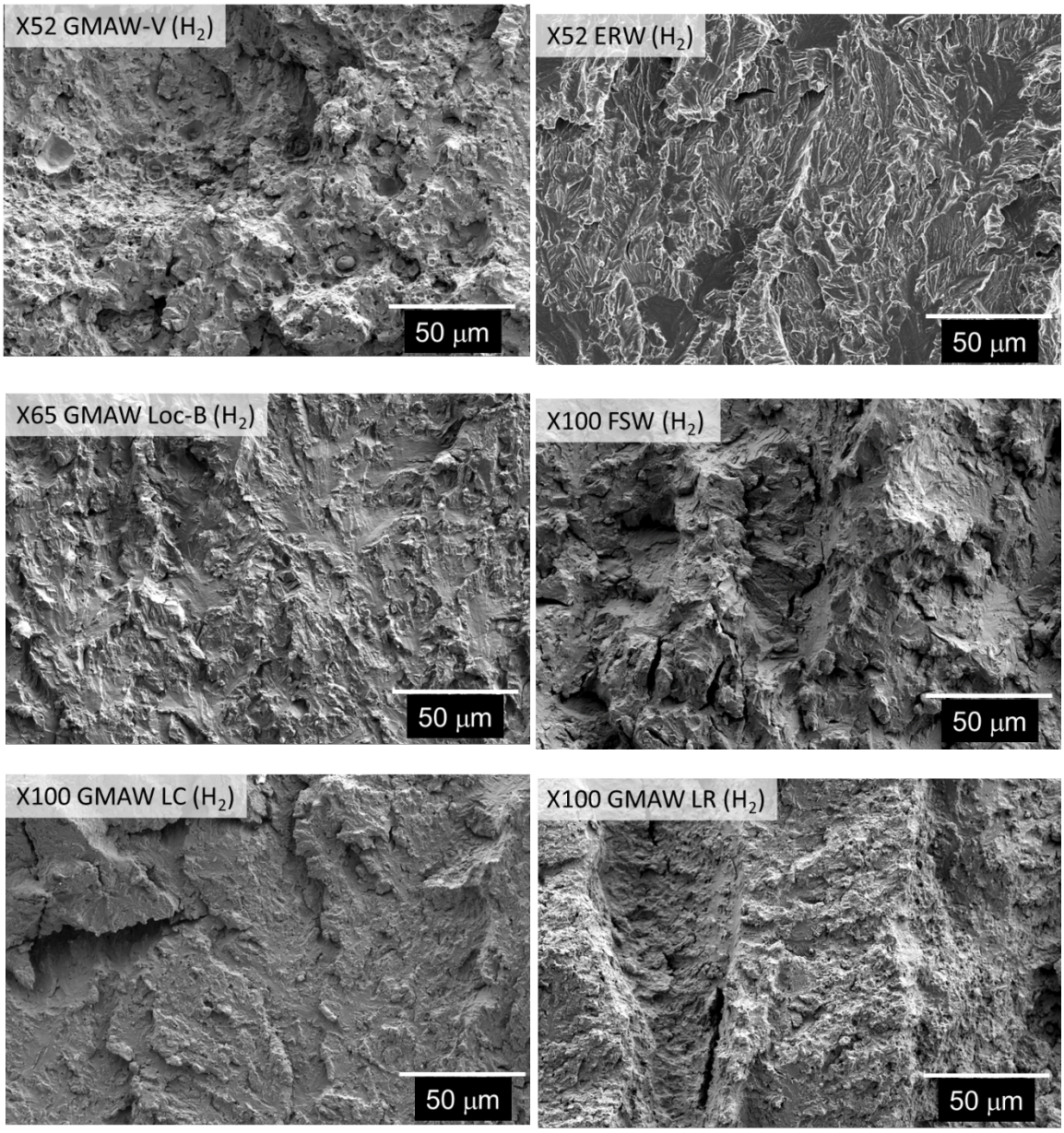

Figure 7 – Scanning electron microscope (SEM) images of fracture surfaces from coupons tested in 21 MPa hydrogen gas. Crack growth direction is from bottom to top in each image.

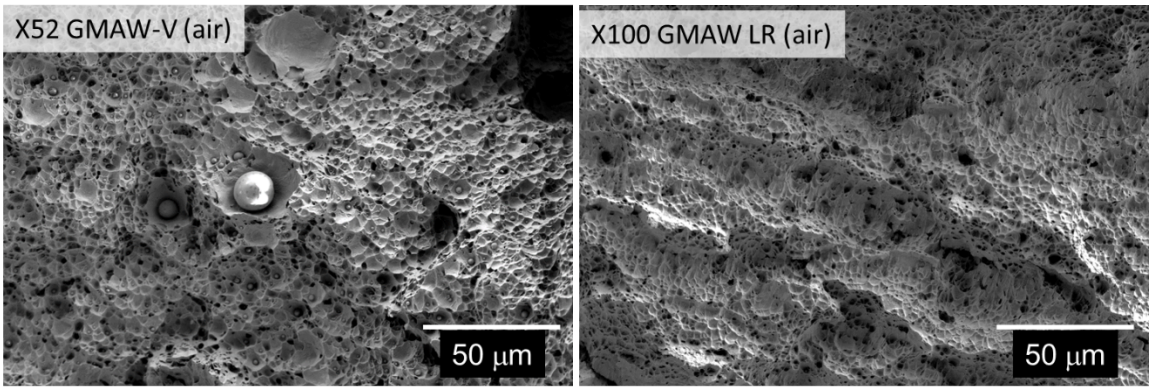

Figure 8 - Scanning electron microscope (SEM) images of fracture surfaces from coupons tested in air of select welds. Crack growth direction is from bottom to top in each image.

4. Discussion

4.1 Test coupon configuration and crack orientation

Obtaining fracture properties of welds can be a challenge as strict dimensional requirements must be satisfied to determine size-independent values. The CT specimen, for example, requires a nominally square coupon, which limits the width dimension, W, in the thickness direction of a pipe. Indeed, the small CT coupons needed to evaluate a crack propagating through the wall of a pipe (e.g., CR and LR orientations) are impractical for ductile steels. Other orientations can be evaluated, where the in-plane dimensions of the CT specimen can be accommodated, such as the LC orientation. Alternatively, other specimen designs may provide more flexibility in certain orientations, such as the arc specimen; however, the arc specimen is not standardized for ductile fracture in ASTM E1820 [27]. For this study, the arc coupon was modified to enable testing of ductile metals by changing the location of the loading pin holes. Additionally, since the arc specimen is not included in elastic-plastic fracture test standards (such as, ASTM E1820), parameters for the analysis of the J-integral must be inferred [27] or models must be developed and vetted to quantitatively determine the parameters for analysis of the J-integral. In this study, we assumed the η-relationship following the guidance in ref [29]. Testing confirmed that the CT and arc coupons give comparable results for X100 base metal tested in gaseous hydrogen at pressure of 21 MPa as shown in Fig. 6a. In 21 MPa hydrogen gas, duplicate tests for arc and CT coupons yielded K_{JH} values of 45 and 49 MPa $m^{1/2}$ for the arc and 45 and 48 MPa $m^{1/2}$ for the CT. The averages of the duplicates for each coupon were the same at 47 MPa $m^{1/2}$, and the differences were less than 5% between all tests. Similarly, X100 base metal arc and CT coupons were tested in air as shown in Fig. 6b which gave a value of 246 MPa $m^{1/2}$ for arc and values of 214, 216, and 225 MPa $m^{1/2}$ for the CT. The largest difference between the values in air for different coupons was less than 15%; however, it is worth noting that only a single arc specimen was tested in air. In [31], fracture resistance was measured on hydrogen-precharged 304L stainless steel using both arc (225, 240, 227, 223, and 220 MPa $m^{1/2}$) and CT (223 and 220 MPa $m^{1/2}$) specimens, identical to the geometries in this present study. The average K_{JH} values were 227 and 222 MPa $m^{1/2}$ for the arc and CT specimens, respectively. The results from [31] demonstrate that the two geometries yield similar fracture resistance at a K_{JH} range that represents the higher values measured in the present study. It appears that the fracture resistance consistency between specimen geometries improves as fracture resistance decreases, which is likely due to lower plasticity in the material with lower fracture resistance. Therefore, we assume that the arc specimen

gives results consistent with the CT coupon for both air or 21 MPa hydrogen tests where the dimensional requirements of equation (1) are satisfied. Therefore, in this study, we directly compare fracture resistance values measured from both specimen geometries.

The arc coupon was used to show that for X100 GMAW, the fracture behavior in the radial direction of the welded pipe (LR) is essentially the same as that along the weld pass direction (i.e. circumferential direction, LC orientation). These two different orientations are shown in Fig. 2d. The fracture toughness was remarkably consistent in air between the two orientations showing negligible difference. Similarly, when tested in 21 MPa hydrogen gas, the measured fracture resistance was nearly identical between the two orientations. The fracture resistance in hydrogen was not measured in multiple orientations for every weld, so broad conclusions cannot be made. However, this result suggests that comparable fracture resistance measurements can be obtained in different orientations if size constraints due to thin pipe walls preclude extraction of coupons in certain orientations, such as cracks growing in the radial direction. This conclusion, however, may not be applicable to highly banded or textured microstructures.

4.2 Welding practice

Fracture resistance clearly decreased in hydrogen gas compared to fracture toughness measurements in air as shown in Fig. 5. The effects of hydrogen on fracture are generally quite substantial and often fracture resistance can be reduced by greater than 50% compared to the fracture toughness in air. Similar reductions of fracture resistance in hydrogen are apparent for both welds and base metals. In all cases, fracture is accompanied by substantial plasticity and should not be described as brittle. With the exception of the highest strength material (X100), the fracture resistance in hydrogen exceeds 60 MPa $m^{1/2}$, and in some cases exceeds 100 MPa $m^{1/2}$.

The X52 GMAW-V weld exhibited relatively low fracture resistance in air compared to the other welds. The large inclusions decorating the fracture surface (Fig. 8) are likely contributing to the low fracture toughness in air. Although a decrease of fracture resistance was observed for X52 GMAW-V weld in hydrogen gas compared to tests in air, the reduction was significantly less compared to the other welds as observed in Fig. 5. This observation could be interpreted in two different ways.

1) The large inclusions influenced the fracture resistance of the X52 GMAW-V regardless of the environment; any further reduction of fracture resistance due to hydrogen was only moderate due to the lower strength. This result is consistent with conclusions from Ref. [15], in which inclusions were identified as governing the fracture resistance of an X80 weld with hydrogen.

2) The large inclusions reduced the fracture toughness in air by directly participating in the microvoid coalescence fracture mode; however, in hydrogen-assisted fracture, the inclusions are not directly involved in the fracture process, appearing only incidentally on the fracture surface. As a result the fracture resistance in hydrogen for X52 GMAW-V is comparable to values for similar strength welds, but its value is relatively high compared to the fracture toughness in air.

In contrast, the X52 ERW displays a slightly lower fracture resistance in hydrogen than the X52 GMAW-V. Whereas this difference is relatively modest (about 10%), the X52 ERW did not show evidence of large inclusions on the fracture surface. In the case of the X52 ERW, a hardness profile across the

welded zone reveals a slightly harder microstructure (Fig. 4). We hypothesize that the hardness of the X52 ERW contributes to the modestly lower fracture resistance compared to the X52 GMAW-V as the general trend is decreasing fracture resistance with increasing strength.

The fracture resistance of X100 FSW appears to be outside the nominal trend, as it displays a relatively low fracture resistance (Fig. 5). A hard zone was identified in the X100 FSW microstructure through microhardness measurements as reported in a previous study on this weld [10]. An overlay of the coupon extraction location on the hardness map (Fig. 9) shows that the crack likely extended through the hard zone, which would then contribute to the lower fracture resistance in hydrogen of the X100 FSW. The microstructure in the hard zone of the X100 FSW was observed to contain bainitic ferrite and likely martensite due to the high hardness [10]. In work on an X80 friction stir weld [19], fracture resistance following electrochemical hydrogen-precharging was observed to be consistently lowest in the hard zone of the weld compared to the stir zone or base metal. These observations suggest that the local microstructure where the crack extended (in the high hardness region) may not be represented by the bulk tensile properties measured from the tensile coupons. In other words, although the tensile results suggested a yield strength of 605 MPa, the local yield strength may be much higher and dominate the fracture response.

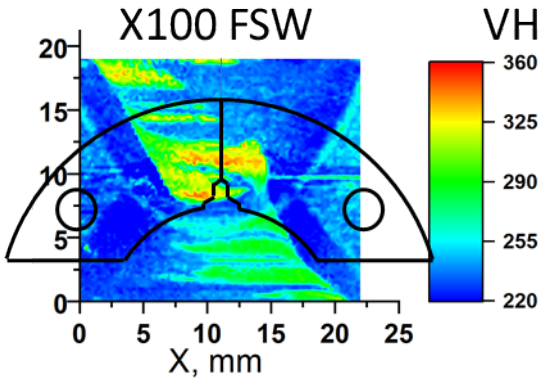

Figure 9 – Microhardness (Vickers (VH)) map of X100 FSW modified from [10] with the arc coupon extraction location. During a fracture test, the crack extended through the hard zone of the microstructure.

4.3 Residual stresses

Residual stresses are a known characteristic of welded components and can impact property measurements [10]. Previous work evaluated the residual stress state in the X65 GMAW [25] as shown in Fig. 10. Here, arc coupons were extracted from two locations in the welds to evaluate the potential effects of residual stress. The coupon from Loc-A was biased towards regions of compressive or low tensile residual stresses based on measured residual stresses in the intact welded pipe (Fig. 10). In contrast, Loc-B is more likely to contain tensile residual stresses. It should be noted that the residual stresses were not measured in the arc coupons but rather inferred based on the location from the measured residual stresses in the intact welded pipe from [25].

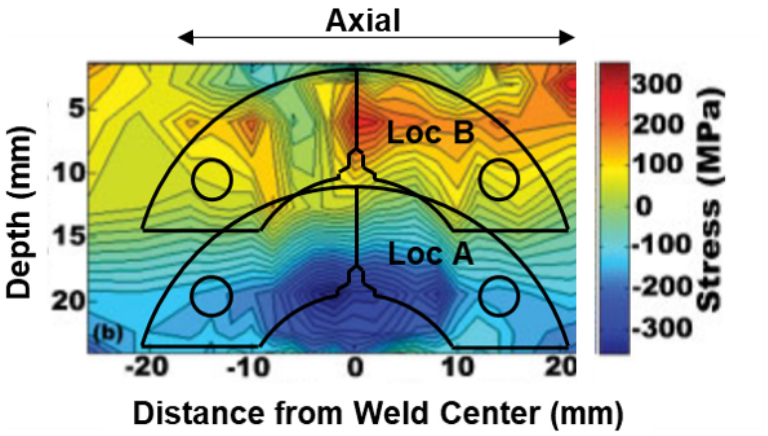

Figure 10 – Measured axial residual stress in X65 GMAW modified from [25] to show the approximate locations of the two arc fracture coupons: Loc-A and Loc-B. Loc-A is predominantly in compressive stressed regions and Loc-B is predominantly in tensile stressed region.

A higher fracture toughness was measured in air in the location with assumed tensile residual stress (Loc-B) compared to the location anticipated to have compressive residual stress (Loc-A). This observation contradicts general expectation and we do not have a clear explanation for this observation. Compressively stressed regions are generally considered less susceptible to fatigue and fracture than tensile stressed regions [10, 32]. Feng *et al.* [32, 33] have made use of compressive residual stresses in welds to improve the apparent fracture resistance and control hydrogen embrittlement. The fracture toughness values measured for the X65 GMAW in both locations were the highest of the materials examined; in particular, the fracture values from Loc-B were not size-independent values due to the limited size of the specimen. Additionally, Loc-B exhibited the greatest scatter of the reported fracture toughness measurements in air, which may point to variations in microstructure, which can affect strength, or residual stress. For the tests in air, more extensive plasticity could relieve the residual stress. The difference in fracture toughness observed between Loc-B and Loc-A may also be due to microstructural variations, where perhaps local hard zones influence the fracture response.

Whereas fracture tests in air do not follow the expected effect of residual stress, fracture measurements in gaseous hydrogen are consistent with anticipated effects of residual stress: tensile residual stresses resulted in a lower average fracture resistance (88 MPa $m^{1/2}$) at Loc-B than at Loc-A with presumed compressive stress (average of 111 MPa $m^{1/2}$). This difference represents a modest effect on fracture resistance of only approximately 26% despite the large difference in residual stress. However, the actual residual stresses in the test coupons are likely much lower [10], offering one potential explanation of this modest difference. For the tests in hydrogen gas, the overall plasticity is reduced, which may still partially relieve the residual stresses, but likely to a lesser extent that the tests in air. Local hardness variations within the weld (as described above for the X100 FSW) and the steep gradient in residual stress provide additional contributing factors that would also influence the relatively modest difference in the fracture resistances at Loc-A and Loc-B.

4.4 Strength

Figure 5 does not show a clear relationship between fracture and strength, particularly for the tests in air, although the general trend is higher strength materials have lower fracture toughness [34].

In order to explore a potential relationship between fracture resistance and strength in gaseous hydrogen environments, Fig. 5 was modified to remove fracture toughness values in air and add pipeline steel data obtained in hydrogen gas at pressure of 21 MPa from the literature [6, 7, 16]. The results are shown in Fig. 11: fracture resistance of the welds tested in this study (closed symbols) compared to base metals (open symbols) from this study and the literature [6-8, 16]. With the exception of X100 FSW, a lower bound trend is apparent for both welds and base metals, where fracture resistance in hydrogen decreases with increasing yield strength. It is notable that welds do not exhibit greater susceptibility to hydrogen-assisted fracture than the base metals, when one compares the results as a function of yield strength; although the fracture resistance was not measured for all base metals. Whereas both the X100 welds showed lower yield strength compared to the base metal, the X100 FSW is an exception to the tendency for lower strength materials to have higher fracture resistance. In contrast, the X100 GMAW displayed a greater fracture resistance than the base metal consistent with the lower bound trend. The lower fracture resistance of the X100 FSW is attributed to local hard spots in the weld. Considering these spots are 30-40% harder than the base metal (Fig. 9), a proportional increase in the local yield strength of this magnitude (to 800-850 MPa) would place the X100 FSW on the general trend.

The welds examined in this study contain a variety of different microstructures, which directly contribute to the differences in strength. Thus, it is difficult to completely separate strength from microstructure in our assessment. It is clear, however, that increased strength resulted in reduced fracture resistance in hydrogen gas. It is also the case that higher strength welds tend to contain microstructural features such as bainitic ferrite and martensite. Since the examined welds do not share similar strengths with different microstructures, it is difficult to make direct conclusions as to the role of microstructural constituents in fracture. In order to identify potential trends with microstructure, it would be necessary to generate different microstructures with nominally the same strength.

In summary, the fracture resistance of pipeline steels in gaseous hydrogen depends on yield strength and the fracture resistance of both welds and base metals follows the same trend; in other words, weld metal does not display greater susceptibility to fracture in gaseous hydrogen than base metals; however, the potential for local hard (or soft) spots should be factored into consideration of weld performance in hydrogen.

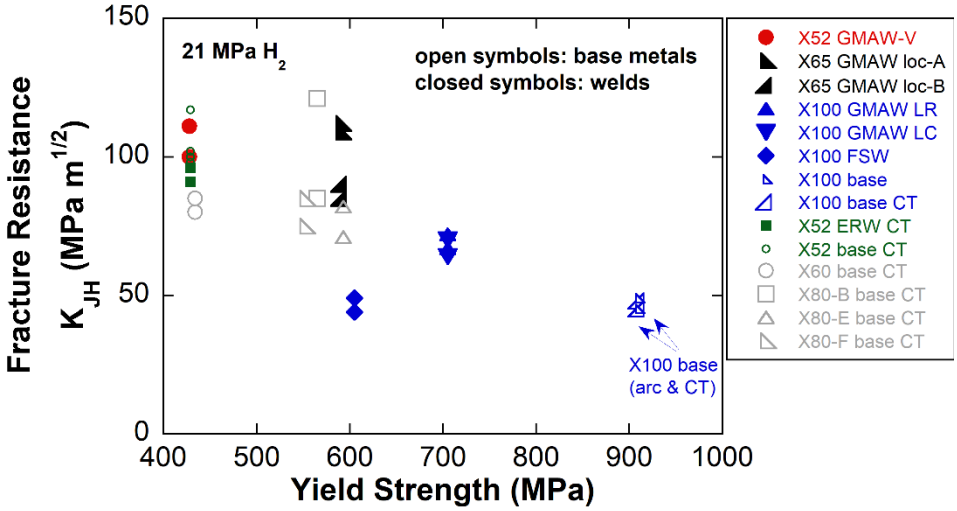

Figure 11 – Fracture resistance (K_{JH}) in 21 MPa hydrogen gas as a function of yield strength for pipeline steel welds and base metals (X60, X80-B, X80-E, X80-F) from the literature [6, 7, 16].

5. Conclusions

Fracture resistance was measured in air and hydrogen gas at pressure of 21 MPa for pipeline steel weld metal from a range of strength grades and welding techniques. All welds exhibited a decrease in fracture resistance in hydrogen compared to complementary tests in air. The general trend was fracture resistance in hydrogen gas at pressure of 21 MPa decreased with increasing yield strength. The results from this study on pipeline steel welds were compared to a variety of pipeline steel base metals from the literature and it was shown that welds tested in hydrogen gas do not appear to exhibit any greater susceptibility to fracture compared to base metals when yield strength is considered. In one notable case, the X100 FSW did exhibit lower fracture resistance in hydrogen than other welds and base metals with similar strength. This lower fracture resistance in hydrogen was attributed to the localized high hardness of the microstructure in the weld zone from where the fracture coupon was extracted. Fracture coupons were located in two different regions in the X65 GMAW, which had previously been characterized by having a gradient in residual stresses from compressive stress at the root to tensile stress at the crown in the welded pipe condition. The expected trend that a coupon located in a compressive stressed region would exhibit a higher fracture toughness was not observed in the tests in air; however, the expected trend did occur in the results from measurements in hydrogen where the fracture resistance was about 26% higher in the compressive stressed location. It should be noted that residual stresses in the test coupons were not measured, but should be significantly lower than in the pipe. It is likely that much of the residual stress is relieved during fracture testing particularly when fracture resistance is high (generally corresponding to substantial plasticity during fracture). Utilization of the arc coupon enabled evaluation of the radially and circumferentially growing cracks in the X100 GMAW, for which no significant difference in fracture properties was observed. Overall, the comparison of welds and base metals from this work suggests that yield strength is the most dominant factor in determining fracture resistance in hydrogen gas and that welds do not generally exhibit greater susceptibility to hydrogen-assisted fracture than the base metals.

6. Acknowledgements

The authors are grateful to B. Davis and J. McNair for support of high pressure testing, A. Gardea, H. Vega for metallographic preparation, and W. York and R. Nishimoto for SEM imaging. Many thanks to our collaborators at the National Institute of Standards and Technology in Boulder, CO, specifically Andrew Slifka and Elizabeth Drexler for many years of sharing materials, ideas, and information. Thanks to our collaborators at Oak Ridge National Laboratory, specifically Zhili Feng and Yanli Wang for fabrication of many of the welds. Sandia National Laboratories is a multimission laboratory managed and operated by National Technology and Engineering Solutions of Sandia, LLC., a wholly owned subsidiary of Honeywell International, Inc., for the U.S. Department of Energy's National Nuclear Security Administration under contract DE-NA-0003525. This work is supported by the U.S. Department of Energy, through the Office of Energy Efficiency and Renewable Energy's (EERE) Hydrogen and Fuel Cell Technologies Office (HFTO). This paper describes objective technical results and analysis. Any

subjective views or opinions that might be expressed in the paper do not necessarily represent the views of the U.S. Department of Energy or the United States Government.

Table 1 – Welded Pipe Dimensions

	Weld Direction	OD (mm)	t (mm)
X52 ERW	Seam	324	12.7
X52 GMAW-V	Girth	914	10.6
X65 GMAW	Girth	508	25.4
X100 GMAW	Girth	1300	19
X100 FSW	Seam	1300	19

Table 2 – Chemical compositions of the pipeline base metals and X52 GMAW-V

Material	C	Mn	P	S	Si	Cu	Ni	Cr	Mo	V	Nb	Ti	Al	B
X52 GMAW-V	0.11	0.35	0.009	0.025	0.1	0.024	0.046	0.018	0.43	0.006	0.001	0.005	0.01	-
X52 V base metal	0.238	0.96	0.011	0.021	0.064	0.085	0.05	0.014	0.004	0.002	0.001	0.002	0.002	-
X52 base metal	0.06	0.87	0.011	0.006	0.12	0.03	0.02	0.03	-	0.002	0.03	-	0.034	-
X65 base metal	0.08	1.53	0.01	0.001	0.32	0.024	0.038	-	-	-	0.039	0.002	-	0.0002
X100 base metal	0.085	1.69	0.013	<0.001	0.26	0.14	0.24	0.19	0.17	-	0.047	0.017	0.029	0.0015

Table 3 - Tensile properties of welds and base metals. Taken from [8, 10, 11, 14, 25].

	Material	Yield stress (MPa)	Tensile stress (MPa)	Orientation
Welds	X52 ERW	*DNM	*DNM	*DNM
	X52 GMAW-V	428	520	C
	X65 GMAW	591	662	L
	X100 GMAW	705	791	L
	X100 FSW	605	780	C
Base Metals	X52	429	493	L
	X52 V	325	526	L
	X65	478	564	L
	X100	910	917	C

*DNM = did not measure

Appendix A - Fracture resistance values for pipeline welds and X100 base metal tested in air (K_{JIC}) and in hydrogen at pressure of 21 MPa (K_{JH})

	Material	Coupon ID	Coupon	Environment	K_{JIC} (MPa $m^{1/2}$)	K_{JH} (MPa $m^{1/2}$)
Welds	X52 GMAW-V	a3	Arc	Air	146	–
	X52 GMAW-V	a5	Arc	Air	138	–
	X52 GMAW-V	a6	Arc	21 MPa	–	111
	X52 GMAW-V	a8	Arc	21 MPa	–	100
	X52 ERW	FT2	CT	21 MPa	–	91
	X52 ERW	FT3	CT	21 MPa	–	96
	X65 GMAW loc-A	bc3	Arc	Air	235	–
	X65 GMAW loc-A	bc4	Arc	Air	234	–
	X65 GMAW loc-A	bc1	Arc	21 MPa	–	109
	X65 GMAW loc-A	bc2	Arc	21 MPa	–	112
	X65 GMAW loc-B	bt2	Arc	Air	*330	–
	X65 GMAW loc-B	bt6	Arc	Air	*299	–
	X65 GMAW loc-B	bt3	Arc	21 MPa	–	85
	X65 GMAW loc-B	bt4	Arc	21 MPa	–	90
	X100 GMAW LR	a1	Arc	Air	148	–
	X100 GMAW LR	a2	Arc	Air	141	–
	X100 GMAW LR	a3	Arc	21 MPa	–	67
	X100 GMAW LR	a4	Arc	21 MPa	–	72
	X100 GMAW LC	b4	Arc	Air	140	–
	X100 GMAW LC	b1	Arc	21 MPa	–	64
	X100 GMAW LC	b2	Arc	21 MPa	–	70
	X100 FSW	b1	Arc	Air	209	–
	X100 FSW	b2	Arc	Air	208	–
	X100 FSW	b3	Arc	21 MPa	–	49
	X100 FSW	b4	Arc	21 MPa	–	44
Base Metals	X52	FT1	CT	21 MPa	–	117
	X52	FT2	CT	21 MPa	–	100
	X52	FT3	CT	21 MPa	–	102
	X52	FT8	CT	21 MPa	–	98
	X100	BM-51	CT	Air	225	–
	X100	BM-52	CT	Air	214	–
	X100	BM8	CT	Air	216	–
	X100	BM11	Arc	Air	246	–
	X100	BM-5	CT	21 MPa	–	48
	X100	BM-64	CT	21 MPa	–	45
	X100	BM12	Arc	21 MPa	–	49
	X100	BM13	Arc	21 MPa	–	45

*J-values were too high to qualify for a valid conversion to K_{JIC} according to Eq. (1). However, the J values were converted to K_{JQ} values for comparison.

References

[1] ASME B31.12-2019. Hydrogen Piping and Pipeline ASME Code fro Pressure Piping ASME, New York, NY, 2019.

[2] Slifka AJ, Drexler ES, Amaro RL, Hayden LE, Stalheim DG, Lauria DS, Hrabe NW. Fatigue measurement of pipeline steels for the application of transporting gaseous hydrogen. J of Pressure Vessel Tech 2017;140:11407-12.

[3] Slifka AJ, Drexler ES, Nanninga NE, Levy YS, McColskey JD, Amaro RL, Stevenson AE. Fatigue crack growth of two pipeline steels in a pressurized hydrogen environment. Corrosion Sci 2014;78:313-21. http://dx.doi.org/10.1016/j.corsci.2013.10.014.

[4] Nanninga NE, Levy YS, Drexler ES, Condon RT, Stevenson AE, Slifka AJ. Comparison of hydrogen embrittlement in three pipeline steels in high pressure gaseous hydrogen environments. Corrosion Sci 2012;59:1-9. http://dx.doi.org/10.1016/j.corsci.2012.01.028.

[5] Ronevich JA, Somerday BP, San Marchi CW. Effects of microstructure banding on hydrogen assisted fatigue crack growth in X65 pipeline steels. Int J of Fatigue 2016;82:497-504. https://doi.org/10.1016/j.ijfatigue.2015.09.004.

[6] San Marchi C, Somerday BP, Nibur KA, Stalheim DG, Boggess T, Jansto S. Fracture resistance and fatigue crack growth of X80 pipeline steel in gaseous hydrogen. Proceedings of ASME 2011 Pressure Vessles & Piping Division Conference, Baltimore, Maryland USA, July 17-21, 2011, 2011.

[7] San Marchi C, Somerday BP, Nibur KA, Stalheim DG, Boggess T, Jansto S. Fracture and fatigue of commercial grade API pipeline steels in gaseous hydrogen. Proceedings of ASME 2010 Pressure Vessels & Piping Division Conference, Bellevue, Washington USA, 2010.

[8] Somerday BP, Sofronis P, Nibur KA, San Marchi C, Kirchheim R. Elucidating the variables affecting accelerated fatigue crack growth of steels in hydrogen gas with low oxygen concentrations. Acta Mater 2013;61:6153-70. http://dx.doi.org/10.1016/j.actamat.2013.07.001.

[9] Ronevich J, Somerday B. Hydrogen-accelerated fatigue crack growth in arc welded X100 pipeline steel. Materials Performance in Hydrogen Environments: Proceedings of the 2016 International Hydrogen Conference, Jackson Hole, WY, B. P. Somerday and P. Sofronis, Eds., 2016: ASME, pp. 219-227.

[10] Ronevich JA, Song EJ, Feng Z, Wang Y, D'Elia C, Hill MR. Fatigue crack growth rates in high pressure hydrogen gas for multiple X100 pipeline welds accounting for crack location and residual stress. Eng Fract Mech 2020;228:106846. https://doi.org/10.1016/j.engfracmech.2019.106846.

[11] Ronevich JA, D'Elia CR, Hill MR. Fatigue crack growth rates of X100 steel welds in high pressure hydrogen gas considering residual stress effects. Eng Fract Mech 2018;194:42-51. https://doi.org/10.1016/j.engfracmech.2018.02.030.

[12] Ronevich JA, Somerday BP, Feng Z. Hydrogen accelerated fatigue crack growth of friction stir welded X52 steel pipe. Int J Hydrogen Energy 2017;42:4259-68. https://doi.org/10.1016/j.ijhydene.2016.10.153.

[13] Ronevich JA, Somerday BP. Assessing gaseous hydrogen assisted fatigue crack growth susceptibility of pipeline steel weld fusion zones and heat affected zones. Materials Performance and Characterization 2016;5:290-304. doi: 10.1520/MPC20150057.

[14] Slifka A, Drexler E, Amaro R, Lauria D, Hayden L, McCowan C, Sowards J. Measurements of fatigue crack growth rates of the heat-affected zones of welds of pipeline steels. Proceedings of ASME 2015 Pressure Vessels and Piping Divison Conference, Boston, MA, 2015.

[15] An T, Zhang S, Feng M, Luo B, Zheng S, Chen L, Zhang L. Synergistic action of hydrogen gas and weld defects on fracture toughness of X80 pipeline steel. Int J Fatigue 2019;120:23-32. https://doi.org/10.1016/j.ijfatigue.2018.10.021.

[16] Ronevich J, San Marchi C, Kolasinski R, Thurmer K, Bartelt N, El Gabaly F, Somerday B. Oxygen impurity effects on hydrogen assisted fatigue and fracture of X100 pipeline steel PVP2018-84163. Proceedings of ASME 2018 Pressure Vessels & Piping Division Conference, Prague, Czech Republic, 2018.
[17] Stalheim D, Boggess T, Bromley D, Jansto S, Ningileri S. Continued microstructure and mechanical property performance evaluation of commercial grade API pipeline steels in high pressure gaseous hydrogen IPC2012-90313. Proceedings of 9th International Pipeline Conference, Calgary, Alberta, Canada, 2012.
[18] Wang Y, Gong J, Jiang W. A quantitative description on fracture toughness of steels in hydrogen gas. Int J of Hydrogen Energy 2013;38:12503-8. https://doi.org/10.1016/j.ijhydene.2013.07.033.
[19] Hoyos JJ, Masoumi M, Pereira VF, Tschiptschin AP, Paes MTP, Avila JA. Influence of hydrogen on the microstructure and fracture toughness of friction stir welded plates of API 5L X80 pipeline steel. Int J Hydrogen Energy 2019;44:23458-71. https://doi.org/10.1016/j.ijhydene.2019.06.210.
[20] Cialone HJ, Holbrook JH. Sensitivity of steels to degradation in gaseous hydrogen. Hydrogen embrittlement: prevention and control, L. Raymond, editor. Philadelphia, PA: ASTM, 1988, pp. 134-151.
[21] Cialone HJ, Holbrook JH. Microstructure and fractographic features of hydrogen-accelerated fatigue crack growth in steels. Microstructural Science 1987;14:407-22.
[22] Cialone HJ, Holbrook JH. Effects of gaseous hydrogen on fatigue crack growth in pipeline steel. Metall Mater Trans A 1985;16:115-22. doi: 10.1007/bf02656719.
[23] Hoover W, Robinson S, Stoltz R, Spingarn J. Hydrogen compatibility of structural materials for energy storage and transmission. Report SAND81-8006. Sandia National Laboratories, Livermore, CA, 1981.
[24] Gutierrez-Solana F, Elices M. High-pressure hydrogen behavior of a pipeline steel. Current Solutions to Hydrogen Problems in Steels. C. Interrante and G. Pressouyre, editors.: American Society of Metals, Metals Park, OH, 1982, pp. 181-185.
[25] T. Neeraj, T. Gnaeupel-Herold, H. Prask, and R. Ayer, "Residual stresses in girth welds of carbon steel pipes: neutron diffraction analysis," Science and Technology of Welding and Joining, vol. 16, no. 3, pp. 249-253, 2011.
[26] ASTM E399. Standard test method for linear-elastic plane-strain fracture toughness K_{IC} of metallic materials. ASTM Int 2020.
[27] ASTM E1820-18a. Standard test method for measurement of fracture toughness. ASTM Int 2018.
[28] San Marchi C, Somerday BP. Technical reference for hydrogen compatibility of materials. Report SAND2012-7321, Sandia National Laboratories, 2012.
[29] Kim Y, Chao YJ, Pechersky MJ, Morgan MJ. C-specimen fracture toughness testing: effect of side grooves and η factor. J Pressure Vessel Technology 2004;126:293-9. doi: 10.1115/1.1762425.
[30] Somerday BP, Campbell JA, Lee KL, Ronevich JA, San Marchi C. Enhancing safety of hydrogen containment components through materials testing under in-service conditions. Int J Hydrogen Energy 2017;42:7314-21. doi: 10.1016/j.ijhydene.2016.04.189.
[31] Ronevich J, San Marchi C, Balch DK. Evaluating the resistance of austenitic stainless steel welds to hydrogen embrittlement, PVP2019-93823. Proceedings of ASME 2019 Pressure Vessels & Piping Division Conference, San Antonio, TX, 2019.
[32] Yu X, Tzelepis DA, Bunn J, Payzant AE, Feng Z. Tensile residual stress mitigation using low temperature phase transformation filler wire in welded armor plates. Materials Research Proceedings 2017;2:461-6. doi: 10.21741/9781945291173-78.
[33] Feng Z, David SA, Demetrios AT, Yu X. Welding method for hydrogen embrittlement control. USA Patent Appl. 14/614,439, 2016.

[34] Nibur K, Somerday B, San Marchi C, Foulk J, Dadfarnia M, Sofronis P. The relationship between crack-tip strain and subcritical cracking thresholds for steels in high-pressure hydrogen gas. Metall Mater Trans A 2012;44A;248-69. doi: 10.1007/s11661-012-1400-5.